A FAST MINIMIZATION ALGORITHM FOR THE EULER ELASTICA MODEL BASED ON A BILINEAR DECOMPOSITION *

ZHIFANG LIU[†], BAOCHEN SUN[†], XUE-CHENG TAI[‡], QI WANG[§], AND HUIBIN CHANG[¶]

Abstract. The Euler Elastica (EE) model with surface curvature can generate artifact-free results compared with the traditional total variation regularization model in image processing. However, strong nonlinearity and singularity due to the curvature term in the EE model pose a great challenge for one to design fast and stable algorithms for the EE model. In this paper, we propose a new, fast, hybrid alternating minimization (HALM) algorithm for the EE model based on a bilinear decomposition of the gradient of the underlying image and prove the global convergence of the minimizing sequence generated by the algorithm under mild conditions. The HALM algorithm comprises three sub-minimization problems and each is either solved in the closed form or approximated by fast solvers making the new algorithm highly accurate and efficient. We also discuss the extension of the HALM strategy to deal with general curvature-based variational models, especially with a Lipschitz smooth functional of the curvature. A host of numerical experiments are conducted to show that the new algorithm produces good results with much-improved efficiency compared to other state-of-the-art algorithms for the EE model. As one of the benchmarks, we show that the average running time of the HALM algorithm is at most one-quarter of that of the fast operator-splitting-based Deng-Glowinski-Tai algorithm.

Key words. Euler Elastica; Hybrid alternating minimization algorithm; Regularization; Bilinear decomposition of the gradient; Curvature-based variational models

MSC codes. 46N10; 47N10; 65K10; 68U10

1. Introduction. We consider solving the Euler Elastica (EE) model numerically for image u defined in $\mathcal{C}^2(\Omega; \mathbb{R})$, $\Omega \subset \mathbb{R}^2$, i.e.,

$$(1.1) \qquad \min_u \int_\Omega \left(a + b \left(\operatorname{div} \frac{\nabla u}{|\nabla u|} \right)^2 \right) |\nabla u| \, dx \, dy + \frac{1}{2} \int_\Omega (u - f)^2 \, dx \, dy,$$

where a and b are two positive parameters, and f is a given noisy image. The first term, known as the EE energy [6, 17, 18], regularizes the lengths and curvatures of the level curves in the image and thus warrants strong continuity of the edges of underlying image u. The second term denotes the fidelity term that measures the difference between given noisy image f and its denoised approximation u. Such a model has been used for image restoration tasks [4, 7, 23]. However, the energy functional in (1.1) has a strongly nonlinear term as well as a singularity at places where the gradient vanishes. This poses a great challenge for one to optimize it.

Traditionally, algorithms for the EE model have been designed directly based on the gradient flow method [6, 22, 28]. The Chan-Kang-Shen (CKS) method [6] used

[†]School of Mathematical Sciences, Tianjin Normal University, Tianjin 300387, China (matlzhf@tjnu.edu.cn, bcsun_tj@163.com).

[‡]Norwegian Research Center (NORCE), Nygårdsgaten 112, 5008 Bergen, Norway (xtai@norceresearch.no).

[§]Department of Mathematics, University of South Carolina, Columbia, SC 29208, USA (qwang@math.sc.edu).

[¶]Corresponding author. School of Mathematical Sciences, Tianjin Normal University, Tianjin 300387, China (changhuibin@tjnu.edu.cn).

a gradient descent scheme for the fourth-order nonlinear Euler-Lagrange equation of the EE model. In order to meet the Courant-Friedrichs-Lewy condition, a small step size needs to be chosen, leading to slow convergence of the CKS method. An accelerated version of the CSK method was proposed by Yashtini and Kang [28] via the Nesterov's technique [19]. Ringhølm, Lazić, and Schönlieb introduced the discrete gradient scheme to the gradient flow of the smooth variant of the EE model based on the Itoh–Abe discrete gradient scheme [22]. Wang et al. [25] proposed efficient scalar auxiliary variable algorithms for more general curvature minimization problems. In order to deal with nonconvexity of (1.1), convex approximations [4] or relaxation methods [5] were used to reformulate the EE energy in higher dimensional spaces. Bredies, Pock, and Wirth in [4] proposed a convex, lower semi-continuous, coercive approximation of the EE energy by functional lifting of the image gradient, and showed some promising results using a tailored discretization of measures. In the work by Chambolle and Pock [5], the EE energy was represented through a convex functional defined on divergence-free vector fields, and successfully applied to diverse shape and image processing tasks utilizing a staggered grid discretization baseed on an averaged Raviart-Thomas finite element approximation.

The variable splitting method was developed to address issues of strong nonlinearity, nonsmoothness, and singularity of (1.1) in [7, 8, 11, 15, 16, 23, 28, 30, 32, 34]. By introducing auxiliary variables, Tai, Hahn, and Chung in [23] proposed a sophisticated relaxation of the EE model and reformulated the energy minimization problem into an equivalent constrained optimization problem, which was then solved by an augmented Lagrangian method [9, 27]. Inspired by this work, there have been extensive studies of variable splitting and augmented Lagrangian method for the EE model. Duan, Wang, and Hahn [8] introduced one more auxiliary variable for the mean curvature and presented a new augmented Lagrangian method. Zhang and Chen in [29] proposed an augmented Lagrangian primal-dual algorithm for the EE model. Yashtini and Kang in [28] relaxed the normal vector in the curvature term of the EE model and developed the relaxed normal two-split (RN2Split) method. Zhang et al. in [30] and Liu et al. in [16] improved the classical augmented Lagrangian method for the EE model via a linearization technique and the proximal method, respectively. Recently, based on the Lie scheme, Deng, Glowinski, and Tai [7] proposed a stable and fast operator-splitting algorithm dubbed the DGT algorithm. Liu and his collaborators extended the DGT algorithm to a color EE model [14] and the Gaussian curvature regularization model [13]. He, Wang, and Chen in [11], adopted a smoothed constrained relaxation model of (1.1) and proposed a convergent penalty relaxation algorithm (dubbed the HWC algorithm) for the discrete EE model.

Although most variable-splitting methods can solve the EE model efficiently, their theoretical convergence is difficult to prove due to the complex relations among the coupled auxiliary variables. Especially in [7], the objective functionals based on the Marchuk–Yanenko scheme [10] for the DGT algorithm are nonsmooth and nonconvex such that it is still unclear how to prove the local convergence to the stationary points of the EE model. Numerical oscillations observed from the relative error (See Figures 4, 5 in [7]) may affect the convergence speed. By introducing an additional auxiliary variable for the Hessian matrix, an operator-splitting algorithm was developed for a more complicated Gaussian-curvature regularized model recently [13], which was also based on the Marchuk–Yanenko scheme. However, a rigorous proof of convergence is still elusive and some numerical oscillations remain. We note that the HWC algorithm guarantees convergence but could inflict a high computational cost. It used the lagged diffusivity fixed point iteration and the scheme for the subproblems has to update the

coefficient matrices per inner loop.

This paper proposes a new convergent variable-splitting algorithm for the EE model (1.1) based on a simple yet powerful regularizing, bilinear decomposition. Notice that gradient ∇u of the underlying image u can be expressed as follows

$$\nabla u = |\nabla u| \frac{\nabla u}{|\nabla u|}.$$

Denoting $q := |\nabla u|$ and $\vec{n} := \frac{\nabla u}{|\nabla u|}$, the gradient is equivalent to the following bilinear decomposition

$$\nabla u = q\vec{n} \qquad \text{with} \quad q \geq 0, \quad |\vec{n}| = 1,$$

with two additional constraints. Using the decomposition, the original EE model can be reformulated as a smooth optimization problem with a non-negative and a unit-length constraint. Namely, the EE energy is expressed by a smooth functional of normal vector $\vec{n}$ and magnitude q. The singularity in the energy disappears and the strong nonlinearity is also mitigated through the bilinear decomposition. When applying it to image denoising, we further simplify the problem by penalizing the bilinear relation, i.e. adding term $\alpha \|\nabla u - q\vec{n}\|^2$ to the energy with a large $\alpha > 0$ instead of imposing the bilinear decomposition through exact penalization or saddle-point problem traditionally used in constrained optimization. This simplification with a fixed $\alpha > 0$ significantly reduces the computational cost.

The reformulation of the EE energy based on a bilinear decomposition of the gradient, relaxation in the constraints through penalties, and the variable splitting technique effectively eliminates the singularity, mitigates the nonlinearity in the original EE model, and improves the regularity of the reformulated energy (objective functional). We then use the finite difference method to discretize the EE energy in space to arrive at a reformulated, discretized EE model. We develop the fast, steadily convergent, hybrid alternating minimization algorithm (HALM) for the discrete EE model. Each subproblem in the new optimization algorithm is solved either in a closed form or approximated efficiently by fast solvers. Under mild conditions, the algorithm is shown to produce a globally convergent minimizing sequence. We discuss the same strategy extended to a list of general curvature-based models, where the corresponding convergence is guaranteed with an $L-$Lipschitz smooth curvature term.

Finally, we conduct a host of experiments to show the effectiveness of the algorithms for image denoising. Compared to the other state-of-the-art algorithms, including the DGT and HWC algorithms, the new algorithm converges much faster for both the EE model and general curvature-based model. In benchmark examples, we show that this algorithm requires only one-quarter of the running time to reach the same given tolerance compared to the other fast operator-splitting-based DGT algorithms. In addition, the algorithm is easy to implement numerically since no staggered grid discretization is needed, and only two algorithmic parameters need to be tuned. This essentially three-step algorithm of low computational complexity and costs has a great potential to be applied to other curvature-based models.

The rest of the paper is organized as follows. Section 2 presents the reformulated model and its discretization. Section 3 provides the proposed algorithm for the reformulated discrete model with a rigorous convergence proof. It is extended to the generalized curvature-based model in section 4. Numerical experiments are conducted in section 5 to validate the proposed algorithm and compare the HALM algorithm

with the other state-of-the-art ones. Finally, we give conclusions and discuss our future work in section 6.

2. Model reformulation and discretization. In this section, we reformulate the EE model (1.1) with a bilinear decomposition and then present its discrete form.

2.1. Reformulation of the EE model. A typical difficulty in dealing with the energy in (1.1) is its weak singularity, i.e. the normal field $\vec{n} = \frac{\nabla u}{|\nabla u|}$ makes no sense at $\{x : |\nabla u(x)| = 0\}$ and may cause numerical instability when the denominator is small. By introducing auxiliary variable q, one can express the gradient ∇u by the bilinear decomposition:

$$(2.1) \qquad \nabla u = q\vec{n}, \ |\vec{n}| = 1, \ q \geq 0,$$

and reformulate EE model (1.1) into the following equivalent minimization problem

$$(2.2) \qquad \min_{u,q,\vec{n}} \int_{\Omega} \left(a + b(\operatorname{div}\vec{n})^2\right)q \,\mathrm{d}x\,\mathrm{d}y + \frac{1}{2}\int_{\Omega}(u-f)^2\,\mathrm{d}x\,\mathrm{d}y$$
$$\text{s.t. } \nabla u = q\vec{n}, \ |\vec{n}| = 1, \ q \geq 0.$$

One may notice that not only does the singularity of the objective functional disappears, but the strong nonlinearity is also mitigated.

We remark that one can extend the bilinear decomposition technique to general curvature-based objective functional [33]

$$(2.3) \qquad \min_{u} \int_{\Omega} \phi(\operatorname{div}(\frac{\nabla u}{|\nabla u|}))|\nabla u|\,\mathrm{d}x\,\mathrm{d}y + \frac{1}{2}\int_{\Omega}(u-f)^2\,\mathrm{d}x\,\mathrm{d}y,$$

with function ϕ (Specific forms will be given in section 4). Based on the bilinear decomposition given in (2.1), one immediately turns the above minimization problem into an equivalent one as follows:

$$(2.4) \qquad \min_{u,\vec{n}} \int_{\Omega} \phi(\operatorname{div}\vec{n})q \,\mathrm{d}x\,\mathrm{d}y + \frac{1}{2}\int_{\Omega}(u-f)^2\,\mathrm{d}x\,\mathrm{d}y,$$
$$\text{s.t. } \nabla u = q\vec{n}, \ |\vec{n}| = 1, \ q \geq 0.$$

2.2. Discretization and penalty relaxation. We consider a meshed rectangle domain: $\Omega = [x_1, x_N] \times [y_1, y_N]$ with mesh sizes $\delta x = (x_N - x_1)/(N-1) = 1$ and $\delta y = (y_N - y_1)/(N-1) = 1$. The corresponding discrete image domain Ω_d is defined by

$$\Omega_d = \{(x_i, y_j) : x_i = x_1 + (i-1)\delta x, y_j = y_1 + (j-1)\delta y, \ i,j = 1,\ldots,N\}.$$

We represent image u as a matrix with entries $u(x_i, y_j)(i,j = 1,\ldots,N)$ defined in Ω_d. For convenience, we rearrange this matrix into a vector $\mathbf{u} = (u_1, u_2, \ldots, u_{N^2})^{\mathrm{T}} \in \mathbb{R}^{N^2}$ by the lexicographical column ordering. Given $\mathbf{n}_1 = (n_{1,1}, n_{1,2}, \ldots, n_{1,N^2})^{\mathrm{T}}$ and $\mathbf{n}_2 = (n_{2,1}, n_{2,2}, \ldots, n_{2,N^2})^{\mathrm{T}}$, belonging to $\mathbb{R}^{N^2}$, we denote $\mathbf{n} := \begin{bmatrix} \mathbf{n}_1 \\ \mathbf{n}_2 \end{bmatrix} \in \mathbb{R}^{2N^2}$. Analogously, vectors $\mathbf{q} \in \mathbb{R}^{N^2}$ and $\mathbf{f} \in \mathbb{R}^{N^2}$ are defined.

We introduce two $N \times N$ matrices $\mathbf{D}_1$ and $\mathbf{D}_2$ as follows

$$\mathbf{D}_1 = \begin{bmatrix} -1 & 1 & & & \\ & -1 & \ddots & & \\ & & & \ddots & 1 \\ 1 & & & & -1 \end{bmatrix}, \ \mathbf{D}_2 = -\mathbf{D}_1^{\mathrm{T}},$$

and four $N^2 \times N^2$ matrices $\mathbf{D}_x^+$, $\mathbf{D}_y^+$, $\mathbf{D}_x^+$ and $\mathbf{D}_y^+$:

$$\mathbf{D}_x^+ = \mathbf{I} \otimes \mathbf{D}_1, \ \ \mathbf{D}_y^+ = \mathbf{D}_1 \otimes \mathbf{I}, \ \ \mathbf{D}_x^- = \mathbf{I} \otimes \mathbf{D}_2, \ \ \mathbf{D}_y^- = \mathbf{D}_2 \otimes \mathbf{I},$$

where $\mathbf{I} \in \mathbb{R}^{N \times N}$ is the identity matrix, and the symbol $\otimes$ denotes the Kronecker product of two matrices. Readily, one can see that

(2.5)
$$\mathbf{D}_x^- = -(\mathbf{D}_x^+)^{\mathrm{T}}, \quad \mathbf{D}_y^- = -(\mathbf{D}_y^+)^{\mathrm{T}}.$$

Assuming the periodic boundary condition for u, we have

$$u(x_1, y_j) = u(x_{N+1}, y_j), \ u(x_i, y_1) = u(x_i, y_{N+1}), \ \ i, j = 1, \ldots, N.$$

Gradient ∇ and divergence div are discretized as follows

$$\nabla \mathbf{u} = \begin{bmatrix} \mathbf{D}_x^+ \mathbf{u} \\ \mathbf{D}_y^+ \mathbf{u} \end{bmatrix} \in \mathbb{R}^{2N^2}, \ \ \mathrm{div}\,\mathbf{n} = \mathbf{D}_x^- \mathbf{n}_1 + \mathbf{D}_y^- \mathbf{n}_2 \in \mathbb{R}^{N^2}.$$

REMARK 2.1. *In variational image processing, the periodic boundary condition is commonly used for historical reasons as well as its benefits in enabling the use of fast discrete Fourier transforms to efficiently solve the linear systems associated with the $\mathbf{u}$-subproblem as in the DGT and HWC algorithms. The Neumann boundary condition could also be a natural choice for boundary conditions. With Neumann boundary conditions, the $\mathbf{u}$-subproblem can be solved via efficient methods like conjugate gradient (CG) descent and sparse Cholesky factorization. In this work, we will primarily use the periodic boundary condition by default. However, we will also explain how to handle Neumann boundary conditions where appropriate.*

Denote the ith row of the matrix $\mathbf{D}_x^-$ (or $\mathbf{D}_y^-$) as $\mathbf{D}_{x,i}^-$ (or $\mathbf{D}_{y,i}^-$). Using the notations above, we obtain the discrete form of (2.2):

(2.6)
$$\min_{\mathbf{u},\mathbf{n},\mathbf{q}} E(\mathbf{u}, \mathbf{n}, \mathbf{q}) = \sum_{i=1}^{N^2} (a + b|\mathbf{D}_{x,i}^- \mathbf{n}_1 + \mathbf{D}_{y,i}^- \mathbf{n}_2|^2) q_i + \frac{1}{2} \|\mathbf{u} - \mathbf{f}\|^2$$
$$\mathrm{s.t.} \ \ \mathbf{D}_x^+ \mathbf{u} = \mathbf{q} \odot \mathbf{n}_1, \ \mathbf{D}_y^+ \mathbf{u} = \mathbf{q} \odot \mathbf{n}_2,$$
$$\mathbf{n}_1 \odot \mathbf{n}_1 + \mathbf{n}_2 \odot \mathbf{n}_2 = \mathbf{1},$$
$$\mathbf{q} \geq \mathbf{0},$$

where $\mathbf{1}$ represents a vector whose elements are all ones, and $\| \cdot \|$ represents the standard ℓ^2 norm, $\odot$ denotes component-wise product, and $\mathbf{q} = (q_1, q_2, \ldots, q_{N^2})^{\mathrm{T}} \geq \mathbf{0}$ denotes the non-negativity of each element. There exists a large family of efficient first-order operator-splitting algorithms [10] to solve discrete model (2.6) with the bilinear constraint.

Instead of strictly enforcing the constraints, we penalize the bilinear constraint in the objective functional and optimize the augmented objective functional using the alternating minimization method. Specifically, we approximate the constrained minimization problem in (2.6) by an unconstrained optimization problem given below

(2.7)
$$\min_{\mathbf{u},\mathbf{n},\mathbf{q}} E_{\alpha,\mathbb{I}}(\mathbf{u}, \mathbf{n}, \mathbf{q}),$$

where

(2.8)
$$E_{\alpha,\mathbb{I}}(\mathbf{u}, \mathbf{n}, \mathbf{q}) = \sum_{i=1}^{N^2} (a + b|\mathbf{D}_{x,i}^- \mathbf{n}_1 + \mathbf{D}_{y,i}^- \mathbf{n}_2|^2) q_i + \frac{1}{2} \|\mathbf{u} - \mathbf{f}\|^2$$
$$+ \frac{\alpha}{2} \left(\|\mathbf{D}_x^+ \mathbf{u} - \mathbf{q} \odot \mathbf{n}_1\|^2 + \|\mathbf{D}_y^+ \mathbf{u} - \mathbf{q} \odot \mathbf{n}_2\|^2 \right)$$
$$+ \mathbb{I}_{\mathcal{S}}(\mathbf{n}) + \mathbb{I}_{\mathbb{R}_+^{N^2}}(\mathbf{q}),$$

$$\mathcal{S} = \left\{ \mathbf{n} = \begin{bmatrix} \mathbf{n}_1 \\ \mathbf{n}_2 \end{bmatrix} : \mathbf{n}_1, \mathbf{n}_2 \in \mathbb{R}^{N^2}, \mathbf{n}_1 \odot \mathbf{n}_1 + \mathbf{n}_2 \odot \mathbf{n}_2 = \mathbf{1} \right\},$$

α is a positive parameter, $\mathbb{R}_+^{N^2} = \{\mathbf{p} \in \mathbb{R}^{N^2} : \mathbf{p} = (p_1, p_2, \ldots, p_{N^2})^{\mathrm{T}}, \ p_i \geq 0, \ \forall i = 1, 2, \cdots, N^2\}$, and the indicator function $\mathbb{I}$ is defined by

$$\mathbb{I}_{\mathcal{A}}(s) = \begin{cases} 0, & \text{if } s \in \mathcal{A}; \\ +\infty, & \text{otherwise.} \end{cases}$$

Theorem 1. *Model* (2.8) *has at least one minimizer.*

The proof of the theorem follows that of theorem 1.4.1 in [21] and is thus omitted. We remark that penalized or relaxation model (2.8) is equivalent to the original model (2.6) only when $\alpha \to \infty$ [20]. In practical use, model (2.8) with a sufficiently large parameter α could generate reasonable denoising results, which is also validated numerically.

3. Hybrid alternating minimization algorithm and its convergence. In this section, we present an efficient hybrid alternating minimization method for problem (2.8) and prove the global convergence of the iterative sequence.

We introduce a smooth function

$$(3.1) \qquad E_\alpha(\mathbf{u}, \mathbf{n}, \mathbf{q}) = \sum_{i=1}^{N^2} (a + b|\mathbf{D}_{x,i}^- \mathbf{n}_1 + \mathbf{D}_{y,i}^- \mathbf{n}_2|^2) q_i + \frac{1}{2} \|\mathbf{u} - \mathbf{f}\|^2$$
$$+ \frac{\alpha}{2} \left(\|\mathbf{D}_x^+ \mathbf{u} - \mathbf{q} \odot \mathbf{n}_1\|^2 + \|\mathbf{D}_y^+ \mathbf{u} - \mathbf{q} \odot \mathbf{n}_2\|^2 \right)$$

to rewrite the objective function in (2.8) as

$$E_{\alpha, \mathbb{I}}(\mathbf{u}, \mathbf{n}, \mathbf{q}) = E_\alpha(\mathbf{u}, \mathbf{n}, \mathbf{q}) + \mathbb{I}_{\mathcal{S}}(\mathbf{n}) + \mathbb{I}_{\mathbb{R}_+^{N^2}}(\mathbf{q}).$$

Note that although $E_{\alpha, \mathbb{I}}$ is nonconvex, it is strongly convex with respect to $\mathbf{u}$ and $\mathbf{q}$, respectively. The projection onto the sphere $\mathcal{S}$ is well-defined. Next, based on the alternating minimization strategy, we present an iterative algorithm to minimize $E_{\alpha, \mathbb{I}}$.

3.1. Hybrid Alternating Minimization Method. We consider solving problem (2.8) by minimizing objective function (2.8) with respect to variables $\mathbf{u}$, $\mathbf{n}$, and $\mathbf{q}$ alternately. Supposing that we have $(\mathbf{u}^k, \mathbf{n}^k, \mathbf{q}^k)$ at the current k-iteration, the proposed **H**ybrid **A**lternating **M**inimization method (HALM) for solving the bilinear decomposition-based EE model (2.8) updates the variables $(\mathbf{u}^{k+1}, \mathbf{n}^{k+1}, \mathbf{q}^{k+1})$ alternatively as follows

$$\begin{cases} \mathbf{u}^{k+1} = \arg\min_{\mathbf{u}} E_{\alpha, \mathbb{I}}(\mathbf{u}, \mathbf{n}^k, \mathbf{q}^k), \\ \mathbf{n}^{k+1} = \arg\min_{\mathbf{n}} \mathbb{I}_{\mathcal{S}}(\mathbf{n}) + \frac{1}{2\tau_k} \|\mathbf{n} - (\mathbf{n}^k - \tau_k \nabla_{\mathbf{n}} E_\alpha(\mathbf{u}^{k+1}, \mathbf{n}^k, \mathbf{q}^k))\|^2, \\ \mathbf{q}^{k+1} = \arg\min_{\mathbf{q}} E_{\alpha, \mathbb{I}}(\mathbf{u}^{k+1}, \mathbf{n}^{k+1}, \mathbf{q}), \end{cases}$$

where τ_k is a positive parameter, E_α is defined in (3.1), and

$$\nabla_{\mathbf{n}} E_\alpha(\mathbf{u}, \mathbf{n}, \mathbf{q}) := \begin{bmatrix} \nabla_{\mathbf{n}_1} E_\alpha(\mathbf{u}, \mathbf{n}, \mathbf{q}) \\ \nabla_{\mathbf{n}_2} E_\alpha(\mathbf{u}, \mathbf{n}, \mathbf{q}) \end{bmatrix} \in \mathbb{R}^{2N^2}.$$

Here, we adopt the forward-backward splitting approach to approximately solve the $\mathbf{n}-$subproblem as

$$\mathbf{n}^{k+1} \approx \min_{\mathbf{n}} E_{\alpha, \mathbb{I}}(\mathbf{u}^{k+1}, \mathbf{n}, \mathbf{q}^k).$$

We will see that each subproblem in the HALM algorithm can be efficiently solved numerically or has a closed-form solution.

The $\mathbf{u}$-subproblem is a standard unconstrained quadratic optimization problem

$$(3.2) \qquad \mathbf{u}^{k+1} = \arg\min_{\mathbf{u}} \ \frac{1}{2}\|\mathbf{u} - \mathbf{f}\|^2 + \frac{\alpha}{2}\big(\|\mathbf{D}_x^+\mathbf{u} - \mathbf{q}^k \odot \mathbf{n}_1^k\|^2$$
$$+ \|\mathbf{D}_y^+\mathbf{u} - \mathbf{q}^k \odot \mathbf{n}_2^k\|^2\big).$$

The unique minimum solution is given by

$$(3.3) \qquad \mathbf{u}^{k+1} = \big(\mathbf{I} \otimes \mathbf{I} + \alpha(\mathbf{D}_x^-\mathbf{D}_x^+ + \mathbf{D}_y^-\mathbf{D}_y^+)\big)^{-1}$$
$$\times \big(\mathbf{f} - \alpha\big(\mathbf{D}_x^-(\mathbf{q}^k \odot \mathbf{n}_1^k) + \mathbf{D}_y^-(\mathbf{q}^k \odot \mathbf{n}_2^k)\big)\big).$$

One readily sees that the positive definite matrix $\mathbf{I} \otimes \mathbf{I} + \alpha(\mathbf{D}_x^-\mathbf{D}_x^+ + \mathbf{D}_y^-\mathbf{D}_y^+)$ is block circulant with circulant blocks (BCCB) such that one can efficiently determine the solution using two-dimensional fast discrete Fourier transform (DFT) [24]. We remark that if assuming the Neumann boundary condition for $\mathbf{u}$, the resulting matrix $\mathbf{I} \otimes \mathbf{I} + \alpha(\mathbf{D}_x^-\mathbf{D}_x^+ + \mathbf{D}_y^-\mathbf{D}_y^+)$ is positive definite as well, such that one can efficiently obtain the solution of (3.3) using efficient methods such as CG and sparse Cholesky factorization.

The $\mathbf{n}$-subproblem is solved by the projection onto the sphere $\mathcal{S}$. From (3.1), one obtain

$$\nabla_{\mathbf{n}_1} E_\alpha(\mathbf{u}^{k+1}, \mathbf{n}^k, \mathbf{q}^k)$$
$$= -2b\mathbf{D}_x^+ \operatorname{diag}(\mathbf{q}^k)(\mathbf{D}_x^-\mathbf{n}_1^k + \mathbf{D}_y^-\mathbf{n}_2^k) + \alpha\mathbf{q}^k \odot (\mathbf{q}^k \odot \mathbf{n}_1^k - \mathbf{D}_x^+\mathbf{u}^{k+1}),$$

where $\operatorname{diag}(\mathbf{q}^k)$ denotes the $N^2 \times N^2$ diagonal matrix with the ith diagonal entry q_i^k. Similarly, one has

$$\nabla_{\mathbf{n}_2} E_\alpha(\mathbf{u}^{k+1}, \mathbf{n}^k, \mathbf{q}^k)$$
$$= -2b\mathbf{D}_y^+ \operatorname{diag}(\mathbf{q}^k)(\mathbf{D}_x^-\mathbf{n}_1^k + \mathbf{D}_y^-\mathbf{n}_2^k) + \alpha\mathbf{q}^k \odot (\mathbf{q}^k \odot \mathbf{n}_2^k - \mathbf{D}_x^+\mathbf{u}^{k+1}).$$

Then denote

$$\mathbf{n}^{k+\frac{1}{2}} := \begin{bmatrix} \mathbf{n}_1^{k+\frac{1}{2}} \\ \mathbf{n}_2^{k+\frac{1}{2}} \end{bmatrix} = \mathbf{n}^k - \tau_k \nabla_{\mathbf{n}} E_\alpha(\mathbf{u}^{k+1}, \mathbf{n}^k, \mathbf{q}^k),$$

where

$$(3.4) \qquad \mathbf{n}_1^{k+\frac{1}{2}} = \mathbf{n}_1^k + \tau_k\big(2b\mathbf{D}_x^+ \operatorname{diag}(\mathbf{q}^k)(\mathbf{D}_x^-\mathbf{n}_1^k + \mathbf{D}_y^-\mathbf{n}_2^k)$$
$$- \alpha\mathbf{q}^k \odot (\mathbf{q}^k \odot \mathbf{n}_1^k - \mathbf{D}_x^+\mathbf{u}^{k+1})\big),$$

$$(3.5) \qquad \mathbf{n}_2^{k+\frac{1}{2}} = \mathbf{n}_2^k + \tau_k\big(2b\mathbf{D}_y^+ \operatorname{diag}(\mathbf{q}^k)(\mathbf{D}_x^-\mathbf{n}_1^k + \mathbf{D}_y^-\mathbf{n}_2^k)$$
$$- \alpha\mathbf{q}^k \odot (\mathbf{q}^k \odot \mathbf{n}_2^k - \mathbf{D}_y^+\mathbf{u}^{k+1})\big).$$

This may not be on the unit sphere. We can project it onto the unit sphere by solving N^2-independent minimization problems:

$$(3.6) \qquad \big[\mathbf{n}^{k+1}\big]_i = \arg\min_{\mathbf{m} \in \mathcal{S}_0^1} \big\|\mathbf{m} - \big[\mathbf{n}^{k+\frac{1}{2}}\big]_i\big\|^2, \ i = 1, 2, \ldots, N^2,$$

where
$$\mathcal{S}_0^1 = \{\mathbf{m} = (m_1, m_2)^{\mathrm{T}} \in \mathbb{R}^2 : m_1^2 + m_2^2 = 1\}.$$

Here, $\left[\mathbf{n}\right]_i = \begin{bmatrix} n_{1,i} \\ n_{2,i} \end{bmatrix}$, where $n_{1,i}$ and $n_{2,i}$ denote ith components of $\mathbf{n}_1$ and $\mathbf{n}_2$, respectively. Each problem in (3.6) has a closed-form solution as follows

$$(3.7) \qquad \left[\mathbf{n}^{k+1}\right]_i = \mathrm{Proj}_{\mathcal{S}_0^1}\left(\left[\mathbf{n}^{k+\frac{1}{2}}\right]_i\right) := \begin{cases} \dfrac{\left[\mathbf{n}^{k+\frac{1}{2}}\right]_i}{\left\|\left[\mathbf{n}^{k+\frac{1}{2}}\right]_i\right\|}, & \text{if } \left[\mathbf{n}^{k+\frac{1}{2}}\right]_i \neq \mathbf{0}, \\ \mathbf{d}, & \text{otherwise}, \end{cases}$$

where $\mathrm{Proj}_{\mathcal{S}_0^1}$ represents the projection operator and $\mathbf{d}$ is an arbitrary unit vector in $\mathcal{S}_0^1$.

The $\mathbf{q}$-subproblem is also separable. For all $i = 1, 2, \ldots, N^2$, let
$$c_i = a + b|\mathbf{D}_{x,i}^- \mathbf{n}_1^{k+1} + \mathbf{D}_{y,i}^- \mathbf{n}_2^{k+1}|^2.$$

Then, q_i-subproblem is described as

$$\begin{aligned} q_i^{k+1} &= \arg\min_{q_i \geq 0} \quad c_i q_i + \frac{\alpha}{2}\left((\mathbf{D}_{x,i}^+ \mathbf{u}^{k+1} - q_i n_{1,i}^{k+1})^2 + (\mathbf{D}_{y,i}^+ \mathbf{u}^{k+1} - q_i n_{2,i}^{k+1})^2\right) \\ &= \arg\min_{q_i \geq 0} \quad c_i q_i + \frac{\alpha}{2} q_i^2 - \alpha q_i(\mathbf{D}_{x,i}^+ \mathbf{u}^{k+1} n_{1,i}^{k+1} + \mathbf{D}_{y,i}^+ \mathbf{u}^{k+1} n_{2,i}^{k+1}), \end{aligned}$$

where the last equation is derived based on the unit length of $\mathbf{n}^{k+1}$. It is 1-dimensional quadratic programming with a nonnegative constraint, and therefore one can directly derive its closed-form solution as follows

$$(3.8) \qquad q_i^{k+1} = \max\left(0, (\mathbf{D}_{x,i}^+ \mathbf{u}^{k+1} n_{1,i}^{k+1} + \mathbf{D}_{y,i}^+ \mathbf{u}^{k+1} n_{2,i}^{k+1}) - \frac{c_i}{\alpha}\right).$$

We summarize the proposed HALM algorithm for solving (2.8) in Algorithm 1.

Algorithm 1 HALM algorithm

Input: The observation image $\mathbf{f}$, the model parameters a, b, the penalty parameter α, and the step size $\{\tau_k\}$.
Output: $\mathbf{u}^k$.
1: Initialization: $k = 0$, $\mathbf{u}^0 = \mathbf{f}$, $\mathbf{n}^0 = \mathrm{Proj}_{\mathcal{S}}\left(((\mathbf{D}_x^+\mathbf{u}^0)^T, (\mathbf{D}_y^+\mathbf{u}^0)^T)^T\right)$, and $q_i^0 = \|(\mathbf{D}_{x,i}^+\mathbf{u}^0, \mathbf{D}_{y,i}^+\mathbf{u}^0)\|$, $i = 1, 2, \ldots, N^2$.
2: **while** The termination condition is not satisfied **do**
3:     Compute $\mathbf{u}^{k+1}$ by (3.3) using 2D FFT.
4:     Compute $\mathbf{n}^{k+1}$ from (3.4), (3.5) and (3.7).
5:     Compute $\mathbf{q}^{k+1}$ via (3.8).
6:     $k \leftarrow k + 1$.
7: **end while**
8: **return** $\mathbf{u}^k$.

In the following section, we will prove the convergence of the HALM algorithm when stepsize τ_k is sufficiently small (say, satisfying (3.13)). For practical use, stepsize τ_k is fixed to a constant heuristically.

3.2. Convergence analysis of HALM. We begin with some useful lemmas.

LEMMA 3.1 (Lemma 3.3 in [31]). *Let $T(\mathbf{x}) = \frac{1}{2}\|\mathbf{A}\mathbf{x} - \mathbf{b}\|^2 + M(\mathbf{x})$, where the function M is convex and the matrix $\mathbf{A}$ is $\mathbf{x}$ -independent. Suppose $\mathbf{x}^*$ is a stationary point of $T(\mathbf{x})$, i.e. $0 \in \partial T(\mathbf{x}^*)$, where $\partial T(\mathbf{x}^*)$ is the subdifferential set of the function T at $\mathbf{x}^*$, then we have*

$$T(\mathbf{x}) - T(\mathbf{x}^*) \geq \frac{1}{2}\|\mathbf{A}(\mathbf{x} - \mathbf{x}^*)\|^2.$$

LEMMA 3.2 (Lemma 2 in [3]). *Consider a composite optimization problem*

$$\min_{\mathbf{x}} \quad \hat{F}(\mathbf{x}) = f_1(\mathbf{x}) + f_2(\mathbf{x}),$$

where $f_2 : \mathbb{R}^n \to \mathbb{R}$ is a continuously differentiable function with gradient ∇f_2 assumed L-Lipschitz continuous, $f_1 : \mathbb{R}^n \to (-\infty, +\infty]$ is a proper and lower semicontinuous (maybe nonsmooth and nonconvex) function with $\inf\{f_1(\mathbf{x}) : \mathbf{x} \in \mathbb{R}^n\} > -\infty$. Let $\{\mathbf{x}^k : k \in \mathbb{N}\}$ be a sequence generated by

$$(3.9) \qquad \mathbf{x}^{k+1} = \mathrm{Prox}_{\tau,f_1}\left(\mathbf{x}^k - \tau\nabla f_2(\mathbf{x}^k)\right)$$

$$:= \arg\min_{\mathbf{x}} f_1(\mathbf{x}) + \frac{1}{2\tau}\|\mathbf{x} - (\mathbf{x}^k - \tau\nabla f_2(\mathbf{x}^k))\|^2.$$

Then one has

$$(3.10) \qquad \frac{1}{2}\left(\frac{1}{\tau} - L\right)\|\mathbf{x}^{k+1} - \mathbf{x}^k\|^2 \leq \hat{F}(\mathbf{x}^k) - \hat{F}(\mathbf{x}^{k+1}).$$

We estimate the Lipschitz constants of the partial derivatives of E_α for the subproblems with respect to single variable $\mathbf{u}$, $\mathbf{q}$, and $\mathbf{n}$, denoted by L_u, L_q, and L_n, respectively. For simplicity, we omit the superscripts and subscripts in the following. The partial derivatives are calculated as follows

$$\nabla_{\mathbf{u}}E_\alpha(\mathbf{u},\mathbf{n},\mathbf{q}) = \mathbf{u} - \mathbf{f} + \alpha\big((\mathbf{D}_x^+)^{\mathrm{T}}(\mathbf{D}_x^+\mathbf{u} - \mathbf{q}\odot\mathbf{n}_1)$$
$$+ (\mathbf{D}_y^+)^{\mathrm{T}}(\mathbf{D}_y^+\mathbf{u} - \mathbf{q}\odot\mathbf{n}_2)\big),$$
$$(3.11) \quad \nabla_{\mathbf{q}}E_\alpha(\mathbf{u},\mathbf{n},\mathbf{q}) = a\mathbf{1} + b|\mathbf{D}_x^-\mathbf{n}_1 + \mathbf{D}_y^-\mathbf{n}_2|^2 + \alpha\big(\mathbf{n}_1\odot(\mathbf{q}\odot\mathbf{n}_1 - \mathbf{D}_x^+\mathbf{u})$$
$$+ \mathbf{n}_2\odot(\mathbf{q}\odot\mathbf{n}_2 - \mathbf{D}_y^+\mathbf{u})\big),$$
$$\nabla_{\mathbf{n}_1}E_\alpha(\mathbf{u},\mathbf{n},\mathbf{q}) = -2b\mathbf{D}_x^+\,\mathrm{diag}(\mathbf{q})(\mathbf{D}_x^-\mathbf{n}_1 + \mathbf{D}_y^-\mathbf{n}_2) + \alpha\mathbf{q}\odot(\mathbf{q}\odot\mathbf{n}_1 - \mathbf{D}_x^+\mathbf{u}),$$
$$\nabla_{\mathbf{n}_2}E_\alpha(\mathbf{u},\mathbf{n},\mathbf{q}) = -2b\mathbf{D}_y^+\,\mathrm{diag}(\mathbf{q})(\mathbf{D}_x^-\mathbf{n}_1 + \mathbf{D}_y^-\mathbf{n}_2) + \alpha\mathbf{q}\odot(\mathbf{q}\odot\mathbf{n}_2 - \mathbf{D}_y^+\mathbf{u}),$$

where $|\cdot|$ denotes the pointwise module operation. From the first two equations in (3.11), we obtain the Lipschitz constants of $\nabla_{\mathbf{u}}E_\alpha$ and $\nabla_{\mathbf{q}}E_\alpha$ (with respect to the variables $\mathbf{u}$ and $\mathbf{q}$) as

$$(3.12) \qquad L_u = \lambda_{\max}\left(\mathbf{I}\otimes\mathbf{I} - \alpha\left(\mathbf{D}_x^-\mathbf{D}_x^+ + \mathbf{D}_y^-\mathbf{D}_y^+\right)\right)$$

and

$$L_q(\mathbf{n}) = \alpha\|\mathbf{n}_1\odot\mathbf{n}_1 + \mathbf{n}_2\odot\mathbf{n}_2\|_\infty,$$

where $\lambda_{\max}(\mathbf{A})$ denotes the largest eigenvalue of the matrix $\mathbf{A}$, and $\|\cdot\|_\infty$ denotes the ℓ^∞ norm in the Euclidean space.

With regard to $\nabla_{\mathbf{n}_1} E_\alpha$ and $\nabla_{\mathbf{n}_2} E_\alpha$, we consider the compound gradient using the last two equations in (3.11)

$$
\begin{aligned}
\nabla_{\mathbf{n}} E_\alpha(\mathbf{u}, \mathbf{n}, \mathbf{q}) &:= \begin{pmatrix} \nabla_{\mathbf{n}_1} E_\alpha(\mathbf{u}, \mathbf{n}, \mathbf{q}) \\ \nabla_{\mathbf{n}_2} E_\alpha(\mathbf{u}, \mathbf{n}, \mathbf{q}) \end{pmatrix} \\
&= \underbrace{\begin{pmatrix} -2b\mathbf{D}_x^+ \operatorname{diag}(\mathbf{q})\mathbf{D}_x^- + \alpha \operatorname{diag}(\mathbf{q})^2 & -2b\mathbf{D}_x^+ \operatorname{diag}(\mathbf{q})\mathbf{D}_y^- \\ -2b\mathbf{D}_y^+ \operatorname{diag}(\mathbf{q})\mathbf{D}_x^- & -2b\mathbf{D}_y^+ \operatorname{diag}(\mathbf{q})\mathbf{D}_y^- + \alpha \operatorname{diag}(\mathbf{q})^2 \end{pmatrix}}_{\mathbf{Q}(\mathbf{q})} \mathbf{n} \\
&\quad + \begin{pmatrix} -\alpha \operatorname{diag}(\mathbf{q})\mathbf{D}_x^+ \mathbf{u} \\ -\alpha \operatorname{diag}(\mathbf{q})\mathbf{D}_y^+ \mathbf{u} \end{pmatrix}.
\end{aligned}
$$

With $\mathbf{q} \geq 0$ (the non-negativity condition), the matrix $\mathbf{Q}(\mathbf{q})$ is positive semidefinite, such that one has

$$
L_n(\mathbf{q}) = \lambda_{\max}(\mathbf{Q}(\mathbf{q})) \geq 0.
$$

Next, we show that the iterative sequence generated by the proposed HALM algorithm has monotonically decreasing objective values.

LEMMA 3.3. *Let the sequence* $\{(\mathbf{u}^k, \mathbf{n}^k, \mathbf{q}^k)\}_{k=1}^{+\infty}$ *be generated by the HALM algorithm with variable stepsize* $\{\tau_k\}_{k=1}^{+\infty}$. *If*

$$
\text{(3.13)} \qquad\qquad 0 < \tau_k \leq \frac{1}{L_n(\mathbf{q}^k)},
$$

the sequence $\{E_{\alpha,\mathbb{I}}(\mathbf{u}^k, \mathbf{n}^k, \mathbf{q}^k)\}_{k=1}^{+\infty}$ *is nonincreasing, i.e.*

$$
\begin{aligned}
&E_{\alpha,\mathbb{I}}(\mathbf{u}^k, \mathbf{n}^k, \mathbf{q}^k) - E_{\alpha,\mathbb{I}}(\mathbf{u}^{k+1}, \mathbf{n}^{k+1}, \mathbf{q}^{k+1}) \\
&\geq \frac{1}{2}(1+\hat{\lambda})\|\mathbf{u}^{k+1} - \mathbf{u}^k\|^2 + \frac{1}{2}\left(\frac{1}{\tau_k} - L_n(\mathbf{q}^k)\right)\|\mathbf{n}^{k+1} - \mathbf{n}^k\|^2 + \frac{\alpha}{2}\|\mathbf{q}^{k+1} - \mathbf{q}^k\|^2,
\end{aligned}
$$

with $\hat{\lambda} := \lambda_{\min}\left(-\alpha(\mathbf{D}_x^- \mathbf{D}_x^+ + \mathbf{D}_y^- \mathbf{D}_y^+)\right)$.

Proof. From Lemma 3.1 and (3.2), we obtain

$$
\text{(3.14)} \qquad E_{\alpha,\mathbb{I}}(\mathbf{u}^k, \mathbf{n}^k, \mathbf{q}^k) - E_{\alpha,\mathbb{I}}(\mathbf{u}^{k+1}, \mathbf{n}^k, \mathbf{q}^k) \geq \frac{1}{2}(1+\hat{\lambda})\|\mathbf{u}^{k+1} - \mathbf{u}^k\|^2.
$$

For $\mathbf{n}_1^{k+1}$ and $\mathbf{n}_2^{k+1}$, it follows from Lemma 3.2

$$
\begin{aligned}
&E_{\alpha,\mathbb{I}}(\mathbf{u}^{k+1}, \mathbf{n}^k, \mathbf{q}^k) - E_{\alpha,\mathbb{I}}(\mathbf{u}^{k+1}, \mathbf{n}^{k+1}, \mathbf{q}^k) \\
\text{(3.15)} \qquad &\geq \frac{1}{2}\left(\frac{1}{\tau_k} - L_n(\mathbf{q}^k)\right)\left(\|\mathbf{n}_1^{k+1} - \mathbf{n}_1^k\|^2 + \|\mathbf{n}_2^{k+1} - \mathbf{n}_2^k\|^2\right).
\end{aligned}
$$

With regard to $\mathbf{q}-$subproblem, for all $i = 1, 2, \cdots, n$, let

$$
\hat{c}_i = c_i - \alpha\left(\mathbf{D}_{x,i}^+ \mathbf{u}^{k+1} n_{1,i}^{k+1} + \mathbf{D}_{y,i}^+ \mathbf{u}^{k+1} n_{2,i}^{k+1}\right).
$$

We have

$$
\text{(3.16)} \qquad \mathbf{q}^{k+1} = \arg\min_{\mathbf{q}} \quad \frac{\alpha}{2}\sum_{i=1}^{N^2}\left((q_i + \frac{\hat{c}_i}{\alpha})^2 + \mathbb{I}_{\mathbb{R}_+}(q_i)\right).
$$

It follows from Lemma 3.1

$$
\text{(3.17)} \qquad E_{\alpha,\mathbb{I}}(\mathbf{u}^{k+1}, \mathbf{n}^{k+1}, \mathbf{q}^k) - E_{\alpha,\mathbb{I}}(\mathbf{u}^{k+1}, \mathbf{n}^{k+1}, \mathbf{q}^{k+1}) \geq \frac{\alpha}{2}\|\mathbf{q}^{k+1} - \mathbf{q}^k\|^2.
$$

Summing up relations (3.14), (3.15) and (3.17), we finally obtain the conclusion. □

We establish the boundedness of the iterative sequence $(\mathbf{u}^k, \mathbf{n}^k, \mathbf{q}^k)$ in the following lemma.

LEMMA 3.4. *Let* $\{(\mathbf{u}^k, \mathbf{n}^k, \mathbf{q}^k)\}_{k=1}^{+\infty}$ *be generated by the HALM algorithm with sufficiently small stepsize satisfying* (3.13). *Then, there exists a positive constant C independent of the index k such that*

$$\max\left\{\|\mathbf{u}^k\|, \|\mathbf{n}^k\|, \|\mathbf{q}^k\|\right\} \leq C. \tag{3.18}$$

Proof. The boundedness of $\{\mathbf{n}^k\}$ is trivial since it is a unit vector. It is readily seen that the functional $E_{\alpha,\mathbb{I}}(\mathbf{u}, \mathbf{n}, \mathbf{q})$ is coercive with respect to $(\mathbf{u}, \mathbf{q})$. It follows from 3.3 $E_{\alpha,\mathbb{I}}(\mathbf{u}^k, \mathbf{n}^k, \mathbf{q}^k)$ is uniformly bounded, implying that $\|\mathbf{u}^k\|_\infty$ and $\|\mathbf{q}^k\|_\infty$ are uniformly bounded. This proves the lemma. $\qquad\square$

Based on the above analysis, we define

$$\gamma = \sup_{k\in\mathbb{N}} L_n(\mathbf{q}^k) < +\infty.$$

In order to study the property of the limit point, we establish an upper bound for the subgradient in the following lemma.

LEMMA 3.5. *There exists* $\mathbf{g}^k := (\mathbf{g}_u^k, \mathbf{g}_n^k, \mathbf{g}_q^k)$ *with*

$$\begin{aligned}
\mathbf{g}_u^k &:= \nabla_{\mathbf{u}} E_\alpha(\mathbf{u}^k, \mathbf{n}^k, \mathbf{q}^k), \\
\mathbf{g}_n^k &\in \nabla_{\mathbf{n}} E_\alpha(\mathbf{u}^k, \mathbf{n}^k, \mathbf{q}^k) + \partial\mathbb{I}_\mathcal{S}(\mathbf{n}^k), \\
\mathbf{g}_q^k &\in \nabla_{\mathbf{q}} E_\alpha(\mathbf{u}^k, \mathbf{n}^k, \mathbf{q}^k) + \partial\mathbb{I}_{\mathbb{R}_+^{N^2}}(\mathbf{q}^k),
\end{aligned}$$

such that

$$\begin{aligned}
\|\mathbf{g}^k\| &\leq \|\mathbf{g}_u^k\| + \|\mathbf{g}_n^k\| + \|\mathbf{g}_q^k\| \\
&\leq 2\alpha\|\mathbf{q}^k - \mathbf{q}^{k-1}\| + \left(2\gamma + \frac{1}{\tau_k}\right)\|\mathbf{n}^k - \mathbf{n}^{k-1}\|.
\end{aligned} \tag{3.19}$$

Proof. For $\mathbf{u}-$subproblem, from the optimality condition of the kth iteration we have

$$\mathbf{0} = \nabla_{\mathbf{u}} E_\alpha(\mathbf{u}^k, \mathbf{n}^{k-1}, \mathbf{q}^{k-1}). \tag{3.20}$$

Based on the estimate of the Lipschitz constant, we have

$$\begin{aligned}
\|\mathbf{g}_u^k\| &= \|\nabla_{\mathbf{u}} E_\alpha(\mathbf{u}^k, \mathbf{n}^k, \mathbf{q}^k)\| \\
&\leq \|\nabla_{\mathbf{u}} E_\alpha(\mathbf{u}^k, \mathbf{n}^k, \mathbf{q}^k) - \nabla_{\mathbf{u}} E_\alpha(\mathbf{u}^k, \mathbf{n}^{k-1}, \mathbf{q}^k)\| \\
&\quad + \|\nabla_{\mathbf{u}} E_\alpha(\mathbf{u}^k, \mathbf{n}^{k-1}, \mathbf{q}^k) - \nabla_{\mathbf{u}} E_\alpha(\mathbf{u}^k, \mathbf{n}^{k-1}, \mathbf{q}^{k-1})\| \\
&\quad + \|\nabla_{\mathbf{u}} E_\alpha(\mathbf{u}^k, \mathbf{n}^{k-1}, \mathbf{q}^{k-1})\| \\
&\leq L_n(\mathbf{q}^k)\|\mathbf{n}^k - \mathbf{n}^{k-1}\| + \alpha\left\|\mathbf{q}^k - \mathbf{q}^{k-1}\right\| \\
&\leq \gamma\|\mathbf{n}^k - \mathbf{n}^{k-1}\| + \alpha\left\|\mathbf{q}^k - \mathbf{q}^{k-1}\right\|.
\end{aligned} \tag{3.21}$$

It follows from Lemma 3.2 that there exists $\mathbf{v}^k \in \partial\mathbb{I}_\mathcal{S}(\mathbf{n}^k)$ such that

$$\|\nabla_{\mathbf{n}} E_\alpha(\mathbf{u}^k, \mathbf{n}^k, \mathbf{q}^{k-1}) + \mathbf{v}^k\| \leq \left(L_n(\mathbf{q}^k) + \frac{1}{\tau_k}\right)\|\mathbf{n}^k - \mathbf{n}^{k-1}\|. \tag{3.22}$$

Denoting $\mathbf{g}_n^k := \nabla_{\mathbf{n}} E_\alpha(\mathbf{u}^k, \mathbf{n}^k, \mathbf{q}^k) + \mathbf{v}^k$ and following (3.22), we have

$$
\begin{aligned}
\|\mathbf{g}_n^k\| &\leq \|\nabla_{\mathbf{n}} E_\alpha(\mathbf{u}^k, \mathbf{n}^k, \mathbf{q}^k) - \nabla_{\mathbf{n}} E_\alpha(\mathbf{u}^k, \mathbf{n}^k, \mathbf{q}^{k-1})\| \\
&\quad + \|\nabla_{\mathbf{n}} E_\alpha(\mathbf{u}^k, \mathbf{n}^k, \mathbf{q}^{k-1}) + \mathbf{v}^k\| \\
&\leq \alpha\|\mathbf{q}^k - \mathbf{q}^{k-1}\| + \left(L_n(\mathbf{q}^k) + \frac{1}{\tau_k}\right)\|\mathbf{n}_1^k - \mathbf{n}^{k-1}\| \\
&\leq \alpha\|\mathbf{q}^k - \mathbf{q}^{k-1}\| + \left(\gamma + \frac{1}{\tau_k}\right)\|\mathbf{n}^k - \mathbf{n}^{k-1}\|.
\end{aligned}
$$
(3.23)

For the $\mathbf{q}$−subproblem, we have

$$
\mathbf{0} \in \nabla_{\mathbf{q}} E_\alpha(\mathbf{u}^k, \mathbf{n}^k, \mathbf{q}^k) + \partial \mathbb{I}_{\mathbb{R}_+^{N^2}}(\mathbf{q}^k).
$$

Then, there exists a $\mathbf{w}^k \in \partial \mathbb{I}_{\mathbb{R}_+^{N^2}}(\mathbf{q}^k)$ such that

$$
\|\mathbf{g}_q^k\| = 0,
$$
(3.24)

where $\mathbf{g}_q^k := \nabla_{\mathbf{q}} E_\alpha(\mathbf{u}^k, \mathbf{n}^k, \mathbf{q}^k) + \mathbf{w}^k$. Summing up (3.21), (3.23), and (3.24), we arrive at the prrof of the lemma. □

Finally, under the condition in Lemma 3.3 and the estimate of the subgradient (bounded by the successive error) in Lemma 3.5, we are ready to prove the convergence of the iterative sequence generated by the HALM algorithm.

Theorem 2. *Let* $\{(\mathbf{u}^k, \mathbf{n}^k, \mathbf{q}^k) : k \in \mathbb{N}\}$ *be a sequence generated by the HALM algorithm with adaptive stepsize* τ^k *satisfying* (3.13). *Then,*
(1) sequence $\{(\mathbf{u}^k, \mathbf{n}^k, \mathbf{q}^k) : k \in \mathbb{N}\}$ *has a finite length, i.e.*

$$
\sum_{k=1}^{+\infty} \|(\mathbf{u}^k, \mathbf{n}^k, \mathbf{q}^k)\| < +\infty;
$$

(2) sequence $\{(\mathbf{u}^k, \mathbf{n}^k, \mathbf{q}^k) : k \in \mathbb{N}\}$ *converges to a critical point of* $E_{\alpha,\mathbb{I}}$.

Proof. It is trivial to show that the objective functional $E_{\alpha,\mathbb{I}}$ is a Kurdyka-Łojasiewicz function [2, 3]. The proof then follows from the proof given in [3]. □

4. Extension to general curvature-based model. In this section, we extend the HALM algorithm to a general curvature-based model [33] given in (2.3). Some examples of function ϕ are given as follows

$$
\phi(\kappa) = \begin{cases} a + b|\kappa|, & \text{total absolute curvature (TAC)}, \\ \sqrt{a + b|\kappa|^2}, & \text{total rotation variation (TRV)}, \\ a + b|\kappa|^2, & \text{total square curvature (TSC)}. \end{cases}
$$

Using the notations given in section 2, one can derive a penalty model for the discrete form of (2.3) as follows

$$
\min_{\mathbf{u}, \mathbf{n}, \mathbf{q}} E_{r,\mathbb{I}}^g(\mathbf{u}, \mathbf{n}, \mathbf{q}),
$$
(4.1)

where

$$
\begin{aligned}
E_{r,\mathbb{I}}^g(\mathbf{u},\mathbf{n},\mathbf{q}) = {} & \sum_{i=1}^{N^2} \phi(\mathbf{D}_{x,i}^- \mathbf{n}_1 + \mathbf{D}_{y,i}^- \mathbf{n}_2)q_i + \frac{1}{2}\|\mathbf{u}-\mathbf{f}\|^2 \\
& + \frac{\alpha}{2}\left(\|\mathbf{D}_x^+\mathbf{u}-\mathbf{q}\odot\mathbf{n}_1\|^2 + \|\mathbf{D}_y^+\mathbf{u}-\mathbf{q}\odot\mathbf{n}_2\|^2\right) \\
& + \mathbb{I}_{\mathcal{S}}(\mathbf{n}) + \mathbb{I}_{\mathbb{R}_+^{N^2}}(\mathbf{q}) \\
:= {} & E_r^g(\mathbf{u},\mathbf{n},\mathbf{q}) + \mathbb{I}_{\mathcal{S}}(\mathbf{n}) + \mathbb{I}_{\mathbb{R}_+^{N^2}}(\mathbf{q}).
\end{aligned}
$$

(4.2)

Note that the HALM algorithm's applicability extends beyond the proposed model. It can directly solve the general form in (2.3) given an $L-$Lipschitz smooth ϕ. Specifically, the TSC case of (2.3) corresponds exactly to the EE model. Moreover, for both TRV and TSC, ϕ satisfies $L-$Lipschitz smoothness and $E_r^g(\mathbf{u},\mathbf{n},\mathbf{q})$ exhibits smoothness. Consequently, the associated models are amenable to direct solution via the HALM algorithm, with the generic scheme given below

$$
\begin{cases}
\mathbf{u}^{k+1} = \arg\min_{\mathbf{u}} E_{r,\mathbb{I}}^g(\mathbf{u},\mathbf{n}^k,\mathbf{q}^k), \\
\mathbf{n}^{k+1} = \arg\min_{\mathbf{n}} \mathbb{I}_{\mathcal{S}}(\mathbf{n}) + \frac{1}{2\tau_k}\|\mathbf{n}-\left(\mathbf{n}^k - \tau_k\nabla_{\mathbf{n}}E_r^g(\mathbf{u}^{k+1},\mathbf{n}^k,\mathbf{q}^k)\right)\|^2, \\
\mathbf{q}^{k+1} = \arg\min_{\mathbf{q}} E_{r,\mathbb{I}}^d(\mathbf{u}^{k+1},\mathbf{n}^{k+1},\mathbf{q}),
\end{cases}
$$

where τ_k is a positive parameter.

For example, if we use the TRV model, its specific iteration scheme is as follows. For the $\mathbf{u}$ and $\mathbf{q}$ subproblems, one solves them exactly the same as in Algorithm 1. For the $\mathbf{n}$-subproblem,

$$
\mathbf{n}^{k+1} = \text{Proj}_{\mathcal{S}}(\mathbf{n}^k - \tau_k\nabla_{\mathbf{n}}E_r^g(\mathbf{u}^{k+1},\mathbf{n}^k,\mathbf{q}^k)),
$$

where

$$
\begin{aligned}
\nabla_{\mathbf{n}_1}E_r^g = {} & b(\mathbf{D}_x^-)^{\text{T}}\left(\frac{\mathbf{q}^k\odot(\mathbf{D}_x^-\mathbf{n}_1^k + \mathbf{D}_y^-\mathbf{n}_2^k)}{\sqrt{a\mathbf{1}+b|\mathbf{D}_x^-\mathbf{n}_1+\mathbf{D}_y^-\mathbf{n}_2|^2}}\right) \\
& + \alpha\mathbf{q}^k\odot(\mathbf{q}^k\odot\mathbf{n}_1^k - \mathbf{D}_x^+\mathbf{u}^{k+1}), \\
\nabla_{\mathbf{n}_2}E_r^g = {} & b(\mathbf{D}_y^-)^{\text{T}}\left(\frac{\mathbf{q}^k\odot(\mathbf{D}_x^-\mathbf{n}_1^k + \mathbf{D}_y^-\mathbf{n}_2^k)}{\sqrt{a\mathbf{1}+b|\mathbf{D}_x^-\mathbf{n}_1+\mathbf{D}_y^-\mathbf{n}_2|^2}}\right) \\
& + \alpha\mathbf{q}^k\odot(\mathbf{q}^k\odot\mathbf{n}_2^k - \mathbf{D}_y^+\mathbf{u}^{k+1}),
\end{aligned}
$$

the notation $\dfrac{\mathbf{p}}{\mathbf{q}}$ denotes the elementwise division of two vectors $\mathbf{p}$ and $\mathbf{q}$, and the projection operator $\text{Proj}_{\mathcal{S}}$ is defined by

$$
[\text{Proj}_{\mathcal{S}}(\mathbf{n})]_i := \text{Proj}_{\mathcal{S}_0^1}([\mathbf{n}]_i) \quad \forall \mathbf{n}\in\mathbb{R}^{2N^2},
$$

for $i=1,2,\cdots,N^2$.

In the TRV model, ϕ is $L-$Lipschitz smooth with respect to variable $\mathbf{n}$, $E_r^g(\mathbf{u},\mathbf{n},\mathbf{q})$ is convex with respect to variables $\mathbf{u}$ and $\mathbf{q}$ respectively, and $E_{r,\mathbb{I}}^d$ is a Kurdyka-Łojasiewicz function. For $\tau_k < \frac{1}{L}$, the above algorithm can be shown to be convergent following the proof of Theorem 2.

We remark that in the nonsmooth case using TAC, a new technique should be developed to design fast convergent algorithms, e.g. introducing more auxiliary variables to deal with the nonsmooth term. We will leave it to our future work.

5. Numerical experiments. In this section, we evaluate the performance of the HALM algorithm via a host of numerical experiments. We implement the HALM algorithm in MATLAB and conduct the numerical experiments on a desktop computer with an Intel i7-6700 CPU and 32GB RAM. First, we compare the algorithm with the DGT algorithm [7] and the HWC algorithm [11] when applied to the EE model for a Gaussian denoising problem. The effects of two algorithmic parameters are discussed as well. Then, we extend the comparison to the speckle denoising problem. Finally, we apply the algorithm to the TRV model for a Gaussian denoising problem.

For the algorithm, we have investigated two different ways to initialize $\mathbf{u}^k$: $\mathbf{u}^0 = \mathbf{0}$ and $\mathbf{u}^0 = \mathbf{f}$. The latter generates better-recovered images than the former $\mathbf{u}^0 = \mathbf{0}$. Hence, we adopt $\mathbf{u}^0 = \mathbf{f}$ as the default in the HALM algorithm. Unless otherwise specified, we stop the HALM algorithm when the relative error of $\mathbf{u}^k$ reaches the prescribed tolerance at

$$(5.1) \qquad \mathrm{ReErr} := \frac{\|\mathbf{u}^{k+1} - \mathbf{u}^k\|}{\|\mathbf{u}^k\|} < tol,$$

where $tol = 10^{-5}$ or the iteration number reaches $N_{\mathrm{iter}} = 500$.

In our experiments, the range of the grey-scale image is limited to $[0, 1]$. We use the peak signal-to-noise ratio (PSNR) and the structural similarity index measure (SSIM) to measure the quality of the restored images. The value of PSNR is defined as

$$\mathrm{PSNR}(\mathbf{u}, \mathbf{u}_c) := 10 \log_{10} \frac{N^2}{\|\mathbf{u} - \mathbf{u}_c\|^2},$$

where $\mathbf{u}$ and $\mathbf{u}_c$ are the recovered image and the ground-truth image, respectively. The value of SSIM is given by

$$\mathrm{SSIM}(\mathbf{u}, \mathbf{u}_c) := \frac{(2\mu_{\mathbf{u}}\mu_{\mathbf{u}_c} + C_1)(2\sigma_{\mathbf{u}\mathbf{u}_c} + C_2)}{(\mu_{\mathbf{u}}^2 + \mu_{\mathbf{u}_c}^2 + C_1)(\sigma_{\mathbf{u}}^2 + \sigma_{\mathbf{u}_c}^2 + C_2)},$$

where $\sigma_{\mathbf{u}}$, $\sigma_{\mathbf{u}_c}$, $\sigma_{\mathbf{u}\mathbf{u}_c}$, $\mu_{\mathbf{u}}$, $\mu_{\mathbf{u}_c}$ denote standard deviations, cross-covariance, and local means of images $\mathbf{u}$ and $\mathbf{u}_c$, respectively, C_1 and C_2 are two constants [26].

5.1. Gaussian denoising by the EE model. In this numerical experiment, we compare the HALM algorithm with two state-of-art algorithms, the DGT and HWC algorithms, to solve the EE model. The eight ground-truth images are shown in Figure 5.1. Images #1 to #5 are synthetic smoothed images, and images #6 to #8 are natural images. We add random noises following the normal distribution $\mathcal{N}(0, 0.0015)$ to these images and then employ the HALM, DGT, and HWC algorithms to denoise the degraded images. The source MATLAB codes of the DGT and HWC algorithms are kindly provided by the authors of [7] and [11], respectively. We set the same maximum number of iterations for the HALM, DGT, and HWC algorithms at $N_{\mathrm{iter}} = 500$. The tolerance of the relative error of $\mathbf{u}^k$ given by (5.1) for the HALM and DGT algorithms is $tol = 10^{-5}$ and that for HWC is $tol = 10^{-4}$. Note that any algorithm that runs for more than 1000 seconds in our experiment will be forced to terminate.

For a fair comparison, we adopt the suggestions for parameter setting of the DGT algorithm in [7] and the HWC algorithm in [11]. It is worth noting that both the DGT
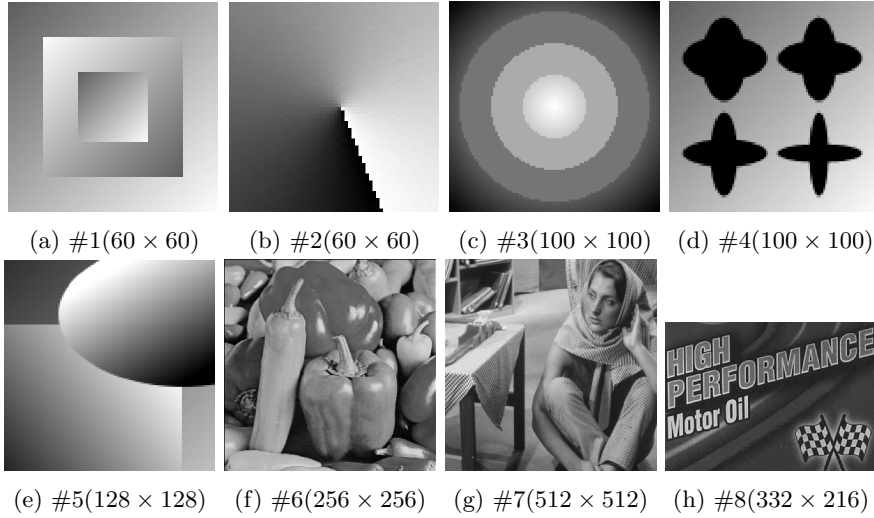
(a) #1(60 × 60)   (b) #2(60 × 60)   (c) #3(100 × 100)   (d) #4(100 × 100)

(e) #5(128 × 128)   (f) #6(256 × 256)   (g) #7(512 × 512)   (h) #8(332 × 216)

Fig. 5.1: Ground-truth images for Gaussian denoising.

Table 5.1: Comparison of the PSNR and SSIM values among the three algorithms.

Image	PSNR			SSIM		
	DGT	HWC	HALM	DGT	HWC	HALM
#1	30.86	33.04	32.93	0.9303	0.9348	0.9317
#2	33.06	35.13	34.63	0.9511	0.9587	0.9664
#3	34.88	36.33	37.33	0.9518	0.9582	0.9629
#4	31.54	32.38	34.48	0.8565	0.8613	0.8795
#5	35.57	38.08	38.09	0.9703	0.9695	0.9697
#6	33.16	/	33.10	0.9071	/	0.9048
#7	31.04	/	31.31	0.8509	/	0.8690
#8	32.47	/	32.39	0.9158	/	0.9019

(a) Noisy   (b) DGT   (c) HWC   (d) HALM
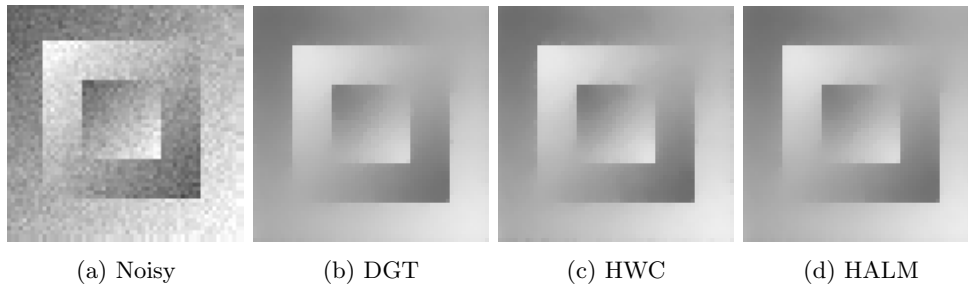
Fig. 5.2: Gaussian denoising results by solving the EE model. (a) The noisy "#1" image with the additive Gaussian noise following $\mathcal{N}(0, 0.0015)$. The denoised images: (b) the DGT algorithm, (c) the HWC algorithm, (d) the proposed HALM algorithm.

Table 5.2: Computational cost comparison among the three algorithms.

| Image	Method	Iterations	Time (sec)	Average time per iteration
#1 (60 × 60)	DGT	171	0.4686	0.0027
	HWC	132	68.3448	0.5178
	HALM	119	0.2099	0.0018
#2 (60 × 60)	DGT	262	0.6378	0.0024
	HWC	113	59.8544	0.5297
	HALM	152	0.2656	0.0017
#3 (100 × 100)	DGT	319	1.8379	0.0058
	HWC	108	213.2229	1.9743
	HALM	220	0.5803	0.0026
#4 (100 × 100)	DGT	447	2.5982	0.0058
	HWC	112	211.2046	1.8858
	HALM	168	0.4346	0.0026
#5 (128 × 128)	DGT	287	2.3686	0.0083
	HWC	90	386.0862	4.2898
	HALM	133	0.4714	0.0035
#6 (256 × 256)	DGT	357	8.9341	0.0250
	HWC	/	/	/
	HALM	184	2.6032	0.0142
#7 (512 × 512)	DGT	256	38.7484	0.1514
	HWC	/	/	/
	HALM	125	8.4747	0.0678
#8 (216 × 332)	DGT	384	12.1821	0.0317
	HWC	/	/	/
	HALM	238	3.7672	0.0158
Average	DGT	310	8.4720	0.0273
	HWC	/	/	/
	HALM	167	2.1009	0.0126
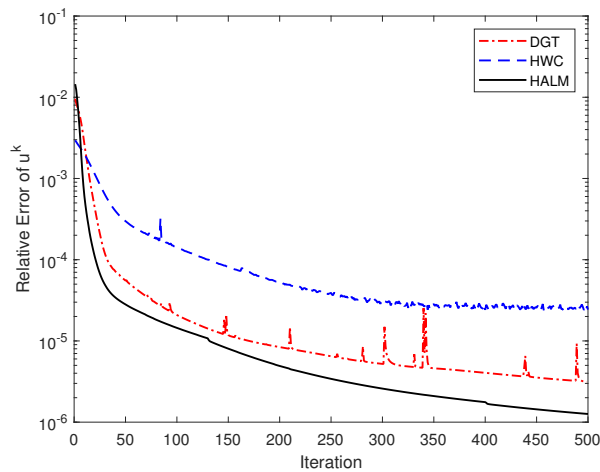
Fig. 5.3: Relative errors of the DGT, HWC, and HALM algorithms. This example is carried out on the #1 image.
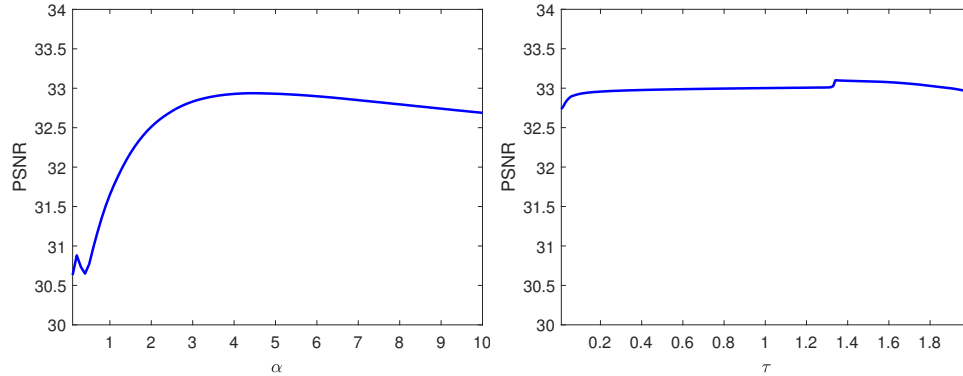
Fig. 5.4: Performances of the proposed HALM under different α and τ. This example is carried out on the #1 image.

and HALM algorithms have four parameters, while the HWC algorithm has nine. We use the strategy of [7] for parameter γ of the DGT algorithm and set parameters at $c = 0.01$, $d = 100$, $\epsilon = 0.01$, $\mu = 0.1$ and $\theta = 0.9$ for the HWC algorithm. We choose $\tau_k = \tau = 0.1$ in the HALM algorithm. For other parameters in the HALM, DGT, and HWC algorithms, we manually tune them to achieve better PSNR values.

Table 5.1 shows the comparison of the PSNR and SSIM values among the three algorithms. The results obtained from the HWC algorithm for images #6, #7, and #8 are missing because the algorithm has been running for over 1000 seconds and hasn't reached the stop criterion. We observe that the HALM algorithm generates comparable high-quality restored images like the DGT and HWC algorithms. The denoised images generated by the HALM, DGT, and HWC algorithms for the #1 image are shown in Figure 5.2.

We record the computational costs, including the total number of iterations and the CPU times, in Table 5.2. The HALM algorithm is the fastest, followed by the DGT and HWC algorithms, respectively. Especially due to the lower computational cost in each iteration and the fewer iterations needed in the HALM algorithm, the average running time in this method is about 1/4 of that in the DGT algorithm. The HWC algorithm is the slowest due to the cost of updating the coefficient matrices in each iteration at each pixel. The computational time of the HWC algorithm increases rapidly with the number of image pixels.

Figure 5.3 presents the evolution of relative errors of $\mathbf{u}^k$ using the DGT, HWC, and HALM algorithms for restoring the #1 image. The relative error of the HALM algorithm decreases as the number of iterations increases, numerically validating the convergence of the algorithm, while the relative error of the DGT algorithm oscillates when its number of iterations exceeds 100. We can also see that the relative error of the HWC algorithm falls off rapidly in the initial 150 iterations, but its numerical convergence rate is lower than that of HALM.

At the end of this part, we conduct the experiment to discuss the algorithmic parameters α and τ in the HALM algorithm. Figure 5.4(a) shows the PSNR values of the recovered #1 image using the HALM algorithm with $\alpha \in [0.1, 10]$. The penalty parameter α in (2.8) should be big enough inferred from Figure 5.4(a), which is consistent with the discussion at the end of section 2. We suggest use parameter α in
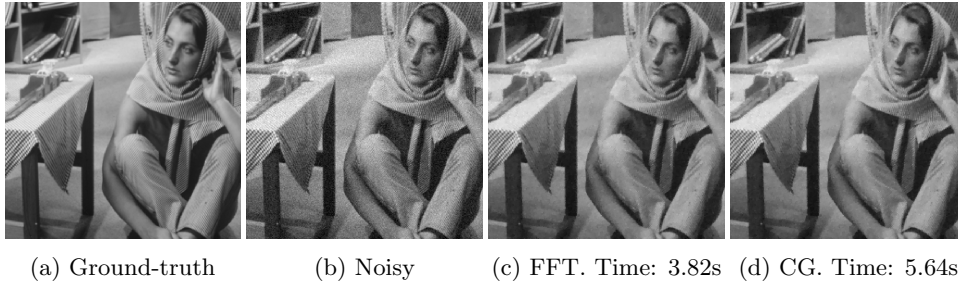
(a) Ground-truth   (b) Noisy   (c) FFT. Time: 3.82s (d) CG. Time: 5.64s

Fig. 5.5: Gaussian denoising results by solving the EE model with different boundary conditions. (a) Ground-truth "barbara" image (256×256). (b) Noisy image with additive Gaussian noise (mean 0, variance 0.0015). (c) Image denoised by HALM algorithm under the periodic boundary condition with PSNR/SSIM values of 31.76/0.8866. (d) Image denoised by HALM algorithm under the Neumann boundary condition with PSNR/SSIM values of 31.78/0.8874.

$[1, 10]$. We also test parameter $\tau \in [0.01, 2]$ and show the PSNR values of the recovered #1 image in Figure 5.4(b). Basically, the parameter τ should be chosen small enough following the condition in Lemma 3.3. Here, we empirically choose $\tau \in [0.1, 1.5]$ with $\tau = 0.1$ as the default.

5.2. Extensive tests. This subsection presents more experiments to demonstrate various aspects of the HALM algorithm. These include examining the effects of different boundary conditions and evaluating the performance of denoising binary, and real color images.

In the first experiment, we discuss the effects of different boundary conditions when using the HALM algorithm to solve the EE model. We compare the performance of the HALM algorithm under periodic and Neumann boundary conditions. For the Neumann case, we solve the u-subproblem using the CG method. The denoising results for the "barbara" image (256×256) are shown in Figure 5.5. The denoised image under the periodic boundary condition achieves a PSNR of 31.76 and an SSIM of 0.8866, while the Neumann boundary condition result has a PSNR of 31.78 and an SSIM of 0.8874. The HALM algorithm produces comparable quantitative results with both boundary conditions. However, the periodic case is faster, with a CPU time of 3.82s, versus 5.64s for the Neumann case. This is because the periodic boundary condition allows using FFT to solve the u-subproblem.

In the second experiment, we apply the HALM algorithm to the EE model to denoise binary images and compare them with the DGT algorithm. We test on a (100×100) "circle" image corrupted by the additive Gaussian noise following $\mathcal{N}(0, 0.1)$, as shown in Figure 5.6 (a) and (b). The denoising results by the DGT and HALM algorithms are displayed in Figure 5.6 (c) and (d). The denoised image by the DGT algorithm has a PSNR of 25.27 and an SSIM of 0.7358, while the HALM algorithm result achieves a PSNR of 26.07 and an SSIM of 0.8194. As the HALM algorithm is a level-set approach, it can effectively preserve the circle shape while removing noise. This demonstrates an advantage over DGT for binary image denoising.

In the third experiment, we employ the HALM algorithm to the EE model to restore real noisy images in standard RGB color spaces from the Smartphone Image
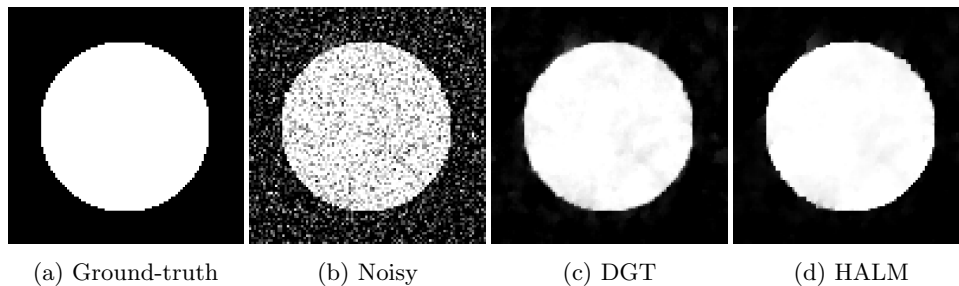
(a) Ground-truth   (b) Noisy   (c) DGT   (d) HALM

Fig. 5.6: Gaussian denoising results of binary images by solving EE model. (a) Ground-truth "circle" image (100×100). (b) Noisy image with additive Gaussian noise (mean 0, variance 0.1), with PSNR/SSIM values of 10.07/0.0953. (c) Image denoised by DGT algorithm with PSNR/SSIM values of 25.27/0.7358. (d) Image denoised by HALM algorithm with PSNR/SSIM values 26.07/0.8194.
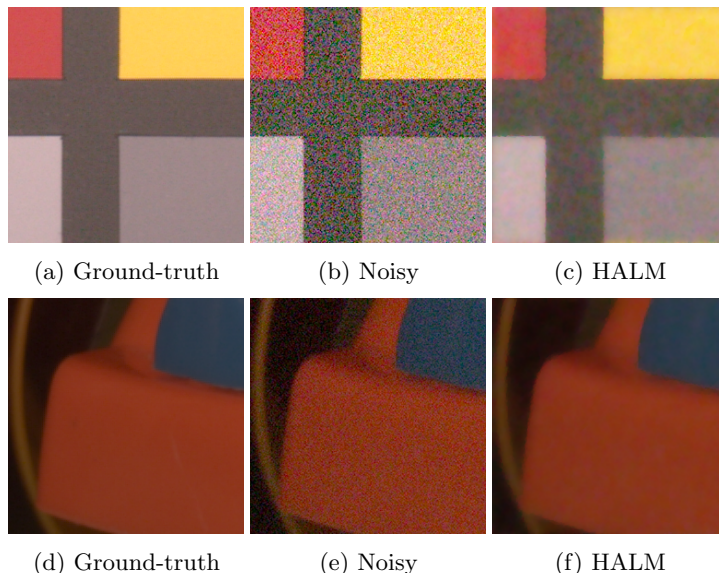

(a) Ground-truth   (b) Noisy   (c) HALM

(d) Ground-truth   (e) Noisy   (f) HALM

Fig. 5.7: Denoising results of real noisy color images by solving EE model with the HALM algorithm. (a) and (d) show the ground-truth images (256×256). (b) and (e) show the noisy images, with PSNR/SSIM values of 18.39/0.4102 and 26.27/0.8755, respectively. (c) and (f) display the denoised images with improved PSNR/SSIM values of 28.69/0.8879 and 36.58/0.9875, respectively.

Table 5.3: Denoising results in average PSNR and SSIM values on the SIDD

Method	SIDD Validation		SIDD Benchmark	
	PSNR	SSIM	PSNR	SSIM
DGT	33.04	0.8895	33.00	0.8860
HALM	33.22	0.8894	33.17	0.8850

(a) Ground-truth   (b) Noisy   (c) HWC   (d) HALM

(e) Zoomed of (a)   (f) Zoomed of (b)   (g) Zoomed of (c)   (h) Zoomed of (d)
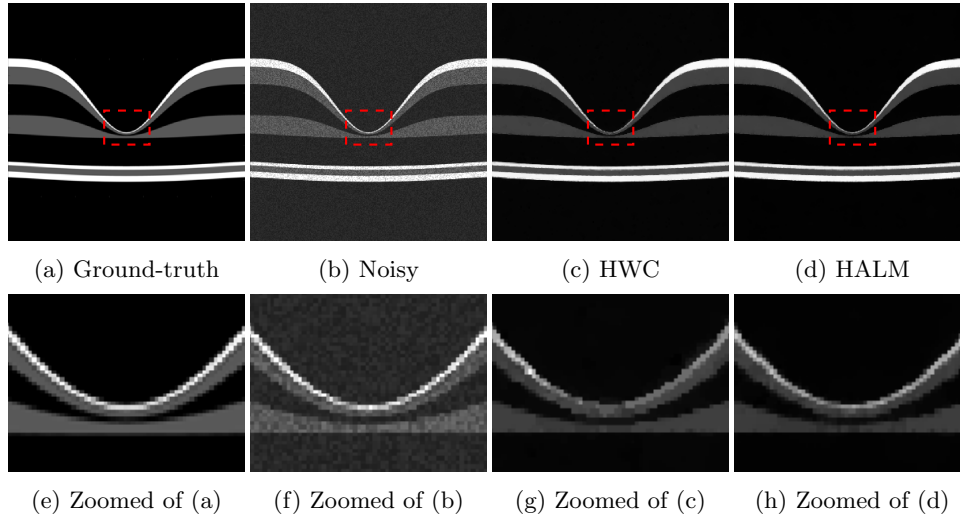
Fig. 5.8: Speckle denoising results for the synthetic OCT image by solving the EE model. First row: (a) Ground-truth OCT image (300×300). (b) Noisy image with multiplicative speckle noise (variance 0.02). (c) Image denoised by HWC algorithm, PSNR = 27.09. (d) Image denoised by proposed HALM algorithm, PSNR = 27.48. Second row: Zoomed views of red boxes in (a), (b), (c), and (d) shown in (e), (f), (g), and (h) respectively.

Denoising Dataset (SIDD) [1]. We first denoise each color channel (R, G, B) separately and then recombine the channels to obtain the final denoised color image. Table 5.3 reports the denoising results in terms of average PSNR and SSIM values over the 1280 noisy image blocks from the SIDD validation data and the 1280 blocks from the SIDD benchmark data. Figure 5.7 (b) and Figure 5.7 (e) display two real noisy images from the SIDD validation data, while Figure 5.7 (a) and Figure 5.7 (d) show their corresponding ground-truth images. Figure 5.7 (c) presents one denoised image with a PSNR value of 26.27 and SSIM value of 0.8755. This denoised image exhibits much-improved quality compared to the original noisy image in Figure 5.7 (b), which has a PSNR of 19.39 and SSIM of 0.4012. The other denoised image in Figure 5.7 (f) with a PSNR of 36.58 and SSIM of 0.9875 also demonstrates significantly enhanced quality over the original noisy image in Figure 5.7 (e), which has a PSNR of 28.69 and SSIM of 0.8879. As shown in Figure 5.7, the HALM algorithm effectively removes noise while preserving features. However, some artificial mosaics can be observed around the edges in the restored image Figure 5.7 (c), likely due to the independent channel-by-channel denoising process. To address this issue, a promising approach would be denoising multiple channels concurrently. We leave the exploration of joint multi-channel denoising with EE energy as future work.

5.3. Speckle denoising. In this experiment, we apply the HALM algorithm to the EE model to denoise the corrupted optical coherence tomography (OCT) image. According to statistical optics, the noise in the OCT image is a multiplicative speckle noise. To recover a high-quality OCT image, we first perform logarithmic compression on the degraded OCT image, which makes the noise in the converted im-
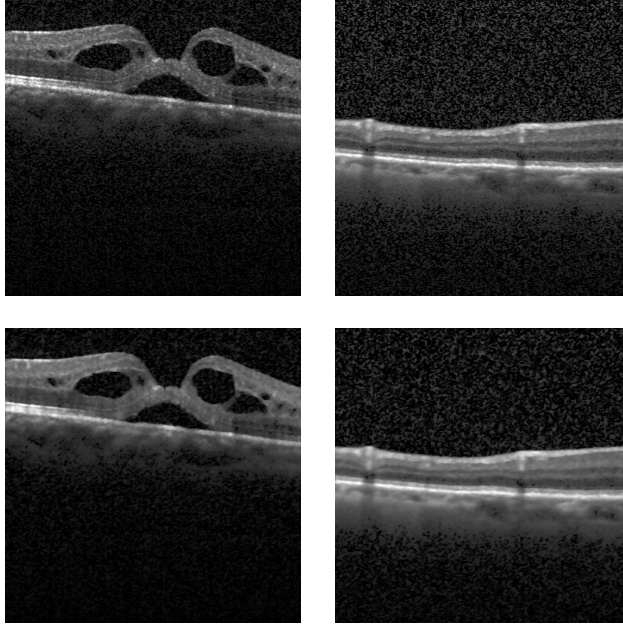
Fig. 5.9: Speckle denoising results for real OCT images by solving the EE model. The first row shows two noisy OCT images (496×496) in the large dataset of labeled OCT and chest X-Ray images [12]. The second row shows the corresponding denoised images by the proposed HALM algorithm.

age additive. We denoise the transformed image by solving the EE model (1.1) with the HALM algorithm. Finally, we obtain the restored OCT image after exponential transformation.

We experiment with a synthetic OCT image generated by the Gaussian function provided in [11]. The variance of the speckle noise is 0.02. The HALM algorithm is compared with the HWC algorithm [11]. Figure 5.8(a) is the ground-truth OCT image, Figure 5.8(b) is the noisy image, and Figure 5.8(c) and (d) are denoised images by the HWC and HALM algorithm for the EE model, respectively. The HALM algorithm performs well at removing the noise and preserving features for the OCT image inferred from Figure 5.8. It renders better PSNR values than the HWC algorithm, since the PSNR value of the denoised image using the HALM algorithm is 27.48, and that using the HWC algorithm is 27.09.

We also test the HALM algorithm on denoising real OCT images from the large dataset of labeled OCT and chest X-ray images [12]. Two representative OCT images are selected from the dataset. The results are shown in Figure 5.9. The noisy images are displayed in the first row, and the corresponding denoised results using the HALM algorithm are shown in the second row. As illustrated in Figure 5.9, the HALM algorithm effectively reduces noise in the regions of interest while preserving important features and anatomical structures in the real OCT images.

5.4. Gaussian denoising by the TRV model. In this experiment, we use the HALM algorithm described in section 4 to solve the TRV model, which is called the HALM-TRV algorithm, and compare it with the discrete total curvature (DTC)
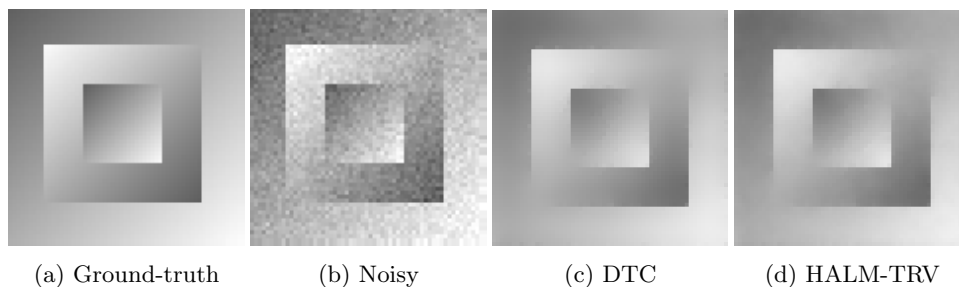
(a) Ground-truth   (b) Noisy   (c) DTC   (d) HALM-TRV

Fig. 5.10: Gaussian denoising results by solving the TRV model. (a) Ground-truth "shading" image (60×60). (b) Noisy image with additive Gaussian noise (mean 0, variance 0.0015). (c) Image denoised by DTC algorithm with PSNR/SSIM values of 32.08/0.9356. (d) Image denoised by HALM-TRV algorithm with PSNR/SSIM values 33.67/0.9410.

algorithm proposed in [33]. The DTC method transfers the TRV model to a re-weighted total variation minimization problem and solves it by the alternating direction method of multipliers (ADMM) based algorithm. The source MATLAB code of the DTC method is kindly provided by the authors of [33]. We experiment with the "shading" image and degrade it with the additive Gaussian noise with a mean of 0 and a variance of 0.0015 (see Figure 5.10 (a) and (b)). We set $a = 0.015$ and $b = 0.005$ in the TRV model. For the HALM-TRV algorithm, we choose $\alpha = 4$ and $\tau = 0.5$. For the DTC algorithm, the parameters are recommended by the authors of [33]. Figure 5.10 (c) and (d) show the denoised images by the HALM-TRV and DTC algorithms, respectively. The DTC algorithm generates a restored image with a PSNR value of 32.08 and an SSIM value of 0.9356, and the HALM-TRV algorithm produces a denoised image with a PSNR value of 33.67 and an SSIM value of 0.9410. We also record the CPU running time of the two algorithms. The CPU time of the DTC algorithm is 1.2900 seconds, and that of the HALM-TRV algorithm is 0.2764 seconds. We notice that the proposed HALM-TRV algorithm outperforms the DTC algorithm in the quality of the denoised image and the computational cost for solving the TRV model.

6. Conclusions. We have proposed a novel bilinear decomposition for the EE model and developed a fast HALM algorithm for its discrete form. We rigorously prove the convergence of the generated minimizing sequence from the algorithm and then validate it numerically. A host of numerical experiments are conducted to demonstrate the performance of the new HALM algorithm in its computation cost and the quality of the recovered images. The proposed algorithm has a great potential for general curvature-based models.

In reference to the latest operator-splitting algorithm presented in [13], we need to point out that the reformulation strategy and the solution method for each subproblem devised for the HALM algorithm are quite different from the strategy developed in [13]. It seems the HALM algorithm cannot be used directly for the Gaussian curvature model to gain its computational efficiency since it will not lead to easy-to-solve sub-minimization problems and thereby lose its computational advantage. Nontrivial splitting technique should be developed. The convergence of the HALM algorithm for the more general models has not yet been established when the smoothness of the ob-

jective function is lacking (e.g. TAC model and the Gaussian curvature regularization model [13]). They will be a part of our future work.

References.

[1] A. ABDELHAMED, S. LIN, AND M. S. BROWN, *A high-quality denoising dataset for smartphone cameras*, in 2018 IEEE/CVF Conference on Computer Vision and Pattern Recognition (CVPR), 2018, pp. 1692–1700, https://doi.org/10.1109/CVPR.2018.00182. (Cited on page 20.)

[2] H. ATTOUCH, J. BOLTE, P. REDONT, AND A. SOUBEYRAN, *Proximal alternating minimization and projection methods for nonconvex problems: An approach based on the Kurdyka-Łojasiewicz inequality*, Mathematics of Operations Research, 35 (2010), pp. 438–457, https://doi.org/10.1287/moor.1100.0449. (Cited on page 12.)

[3] J. BOLTE, S. SABACH, AND M. TEBOULLE, *Proximal alternating linearized minimization for nonconvex and nonsmooth problems*, Mathematical Programming, 146 (2013), https://doi.org/10.1007/s10107-013-0701-9. (Cited on pages 9 and 12.)

[4] K. BREDIES, T. POCK, AND B. WIRTH, *A convex, lower semicontinuous approximation of Euler's elastica energy*, SIAM Journal on Mathematical Analysis, 47 (2015), pp. 566–613, https://doi.org/10.1137/130939493. (Cited on pages 1 and 2.)

[5] A. CHAMBOLLE AND T. POCK, *Total roto-translational variation*, Numerische Mathematik, 142 (2019), pp. 611–666, https://doi.org/10.1007/s00211-019-01026-w. (Cited on page 2.)

[6] T. F. CHAN, S. H. KANG, AND J. SHEN, *Euler's elastica and curvature-based inpainting*, SIAM Journal on Applied Mathematics, 63 (2002), pp. 564–592, https://doi.org/10.1137/S0036139901390088. (Cited on page 1.)

[7] L.-J. DENG, R. GLOWINSKI, AND X.-C. TAI, *A new operator splitting method for the Euler elastica model for image smoothing*, SIAM Journal on Imaging Sciences, 12 (2019), pp. 1190–1230, https://doi.org/10.1137/18M1226361. (Cited on pages 1, 2, 14, and 17.)

[8] Y. DUAN, Y. WANG, X.-C. TAI, AND J. HAHN, *A fast augmented Lagrangian method for Euler's ealstica model*, Numerical Mathematics: Theory, Methods and Applications, 6 (2012), pp. 47–71, https://doi.org/10.4208/nmtma.2013.mssvm03. (Cited on page 2.)

[9] R. GLOWINSKI AND P. LE TALLEC, *Augmented Lagrangian and operator-splitting methods in nonlinear mechanics*, SIAM, 1989. (Cited on page 2.)

[10] R. GLOWINSKI, S. OSHER, AND W. YIN, eds., *Splitting Methods in Communication, Imaging, Science, and Engineering*, Springer-Verlag New York, 2016. (Cited on pages 2 and 5.)

[11] F. HE, X. WANG, AND X. CHEN, *A penalty relaxation method for image processing using Euler's elastica model*, SIAM Journal on Imaging Sciences, 14 (2021), pp. 389–417, https://doi.org/10.1137/20M1335601. (Cited on pages 2, 14, and 21.)

[12] D. S. KERMANY, M. GOLDBAUM, W. CAI, ET AL., *Identifying medical diagnoses and treatable diseases by image-based deep learning*, Cell, 172

(2018), pp. 1122–1131.e9, https://doi.org/https://doi.org/10.1016/j.cell.2018.02.010. (Cited on page 21.)

[13] H. Liu, X.-C. Tai, and R. Glowinski, *An operator-splitting method for the Gaussian curvature regularization model with applications to surface smoothing and imaging*, SIAM Journal on Scientific Computing, 44 (2022), pp. A935–A963, https://doi.org/10.1137/21M143772X. (Cited on pages 2, 22, and 23.)

[14] H. Liu, X.-C. Tai, R. Kimmel, and R. Glowinski, *A color elastica model for vector-valued image regularization*, SIAM Journal on Imaging Sciences, 14 (2021), p. 717–748, https://doi.org/10.1137/20M1354532. (Cited on page 2.)

[15] Z. Liu, Y. Duan, C. Wu, and X.-C. Tai, *On variable splitting and augmented lagrangian method for total variation-related image restoration models*, in Handbook of Mathematical Models and Algorithms in Computer Vision and Imaging, K. Chen, C.-B. Schönlieb, X.-C. Tai, and L. Younces, eds., Springer International Publishing, Cham, 2021, pp. 1–47, https://doi.org/10.1007/978-3-030-03009-4_84-2. (Cited on page 2.)

[16] Z. Liu, S. Wali, Y. Duan, H. Chang, C. Wu, and X.-C. Tai, *Proximal ADMM for Euler's elastica based image decomposition model*, Numerical Mathematics: Theory, Methods and Applications, 12 (2019), pp. 370–402, https://doi.org/10.4208/nmtma.OA-2017-0149. (Cited on page 2.)

[17] S. Masnou and J.-M. Morel, *Level lines based disocclusion*, in Proceedings 1998 International Conference on Image Processing. ICIP98 (Cat. No.98CB36269), IEEE Comput. Soc, 1998, https://doi.org/10.1109/icip.1998.999016. (Cited on page 1.)

[18] D. Mumford, *Elastica and computer vision*, in Algebraic geometry and its applications, Springer, 1994, pp. 491–506. (Cited on page 1.)

[19] Y. E. Nesterov, *A method for solving the convex programming problem with convergence rate $O(1/k^2)$ (in russian)*, in Dokl. Akad. Nauk SSSR, vol. 269, 1983, pp. 543–547. (Cited on page 2.)

[20] J. Nocedal and S. J. Wright, *Numerical Optimization*, Springer New York, NY, 2nd ed., 2006. (Cited on page 6.)

[21] A. L. Peressini, F. E. Sullivan, and J. J. Uhl, *The Mathematics of Nonlinear Programming*, Springer-Verlag New York, 1988. (Cited on page 6.)

[22] T. Ringhølm, J. Lazić, and C. Schönlieb, *Variational image regularization with Euler's elastica using a discrete gradient scheme*, SIAM Journal on Imaging Sciences, 11 (2018), pp. 2665–2691, https://doi.org/10.1137/17M1162354. (Cited on pages 1 and 2.)

[23] X.-C. Tai, J. Hahn, and G. J. Chung, *A fast algorithm for Euler's elastica model using augmented Lagrangian method*, SIAM Journal on Imaging Sciences, 4 (2011), p. 313–344, https://doi.org/10.1137/100803730. (Cited on pages 1 and 2.)

[24] C. R. Vogel, *Computational methods for inverse problems*, SIAM, 2002. (Cited on page 7.)

[25] C. Wang, Z. Zhang, Z. Guo, T. Zeng, and Y. Duan, *Efficient SAV algorithms for curvature minimization problems*, IEEE Transactions on Circuits and Systems for Video Technology, (2022), https://doi.org/10.1109/TCSVT.2022.3217586. (Cited on page 2.)

[26] Z. Wang, A. Bovik, H. Sheikh, and E. Simoncelli, *Image quality assessment: From error visibility to structural similarity*, IEEE Transactions on Image Processing, 13 (2004), pp. 600–612, https://doi.org/10.1109/TIP.2003.819861. (Cited on page 14.)

[27] C. Wu and X.-C. Tai, *Augmented Lagrangian method, dual methods, and split*

Bregman iteration for ROF, vectorial TV, and high order models, SIAM Journal on Imaging Sciences, 3 (2010), pp. 300–339, https://doi.org/10.1137/090767558. (Cited on page 2.)

[28] M. Yashtini and S. H. Kang, *A fast relaxed normal two split method and an effective weighted TV approach for Euler's elastica image inpainting*, SIAM Journal on Imaging Sciences, 9 (2016), pp. 1552–1581, https://doi.org/10.1137/16M1063757. (Cited on pages 1 and 2.)

[29] J. Zhang and K. Chen, *A new augmented Lagrangian primal dual algorithm for elastica regularization*, Journal of Algorithms & Computational Technology, 10 (2016), pp. 325–338, https://doi.org/10.1177/1748301816668044. (Cited on page 2.)

[30] J. Zhang, R. Chen, C. Deng, and S. Wang, *Fast linearized augmented Lagrangian method for Euler's elastica model*, Numerical Mathematics: Theory, Methods and Applications, 10 (2017), pp. 98–115, https://doi.org/10.4208/nmtma.2017.m1611. (Cited on page 2.)

[31] J. Zhang, Y. Duan, Y. Lu, M. K. Ng, and H. Chang, *Bilinear constraint based ADMM for mixed Poisson-Gaussian noise removal*, Inverse Problems & Imaging, 15 (2021), pp. 339–366, https://doi.org/10.3934/ipi.2020071. (Cited on page 9.)

[32] Y. Zhang, S. Li, Z. Guo, B. Wu, and S. Du, *Image multiplicative denoising using adaptive Euler's elastica as the regularization*, Journal of Scientific Computing, 90 (2022), p. 69, https://doi.org/10.1007/s10915-021-01721-7. (Cited on page 2.)

[33] Q. Zhong, Y. Li, Y. Yang, and Y. Duan, *Minimizing discrete total curvature for image processing*, in 2020 IEEE/CVF Conference on Computer Vision and Pattern Recognition (CVPR), 2020, pp. 9471–9479, https://doi.org/10.1109/CVPR42600.2020.00949. (Cited on pages 4, 12, and 22.)

[34] W. Zhu, X. C. Tai, and T. Chan, *Image segmentation using Euler's elastica as the regularization*, Journal of Scientific Computing, 57 (2013), pp. 414–438, https://doi.org/10.1007/s10915-013-9710-3. (Cited on page 2.)